ACSNANO

www.acsnano.org

ARTICLE

Amorphizing Metal Selenides-Based ROS Biocatalysts at Surface Nanolayer toward Ultrafast Inflammatory Diabetic Wound Healing

Yuting Deng,[⊥] Yang Gao,[⊥] Tiantian Li, Sutong Xiao, Mohsen Adeli, Raul D. Rodriguez, Wei Geng,* Qiu Chen,* Chong Cheng,* and Changsheng Zhao

Cite This: *ACS Nano* 2023, 17, 2943−2957

Read Online

ACCESS | Metrics & More | Article Recommendations | Supporting Information

ABSTRACT: **The microenvironments with high reactive-oxygen-species (ROS) levels, inflammatory responses, and oxidative-stress effects in diabetic ulcer wounds, leading to poor proliferation and differentiation of stem cells, severely inhibit their efficient healing. Here, to overcome the unbalanced multielectron reactions in ROS catalysis, we develop a cobalt selenide-based biocatalyst with an amorphous Ru@CoSe nanolayer for ultrafast and broad-spectrum catalytic ROS-elimination. Owing to the enriched electrons and more unoccupied orbitals of Ru atoms, the amorphous Ru@CoSe nanolayer-equipped biocatalyst displays excellent catalase-like kinetics (maximal reaction velocity, 23.05 μM s^{-1}; turnover number, 2.00 s^{-1}), which exceeds most of the currently reported metal compounds. The theoretical studies show that Ru atoms act as "regulators" to tune the electronic state of the Co sites and modulate the interaction of oxygen intermediates, thus improving the reversible redox properties of active sites. Consequently, the Ru@CoSe can efficiently rescue the proliferation of mesenchymal stem cells and maintain their angiogenic potential in the oxidative stress environment. *In vivo* experiments reveal the superior ROS-elimination ability of Ru@CoSe on the inflammatory diabetic wound. This study offers an effective nanomedicine for catalytic ROS-scavenging and ultrafast healing of inflammatory wounds and also provides a strategy to design biocatalytic metal compounds *via* bringing amorphous catalytic structures.**

KEYWORDS: *metal selenides, ROS-scavenging materials, ROS biocatalysis, diabetic wound healing, tissue regeneration*

INTRODUCTION

Diabetic ulcer with an inflammatory and refractory wound is one of the complications of diabetes that significantly increases the amputation rate and mortality of diabetic patients.[1,2] The highly limited self-recovery capacity and the complexity and susceptibility of the lesion area (up-regulated pro-inflammatory factors, hyperglycemia, hypoxia, overexpression reactive oxygen species (ROS), vascular lesions, *etc.*) create great challenges for diabetic ulcer therapy.[3−8] The traditional clinical treatments, such as hyperbaric oxygen therapy, glycemic control, and anti-infection by antibiotics, can alleviate hypoxia and vascular lesions in the ulcer area to some degree.[9−12] However, their low healing rate and high recurrence rate make the vast

Received: November 16, 2022
Accepted: January 17, 2023
Published: January 23, 2023

https://doi.org/10.1021/acsnano.2c11448
ACS Nano 2023, 17, 2943−2957

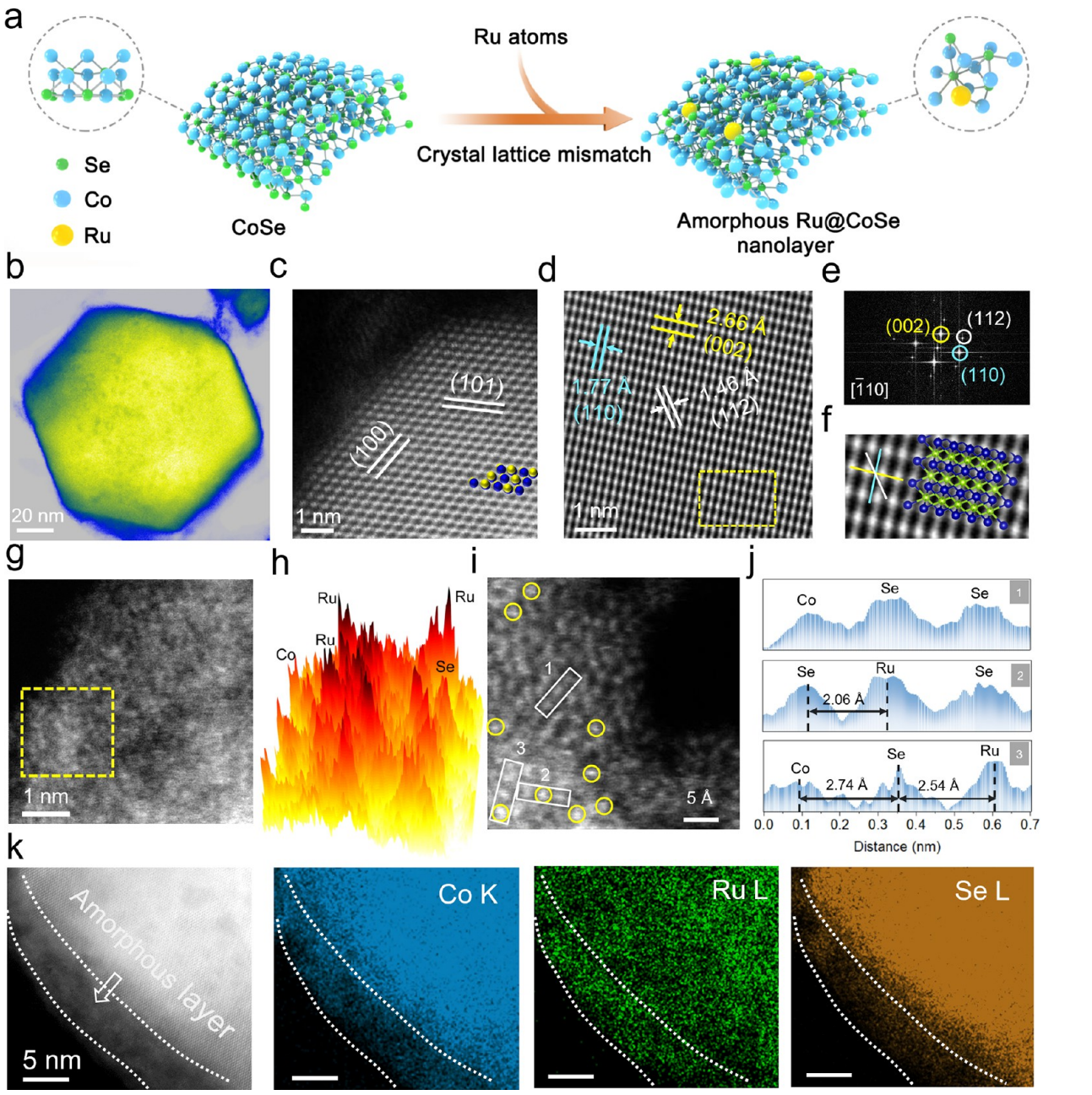

Figure 1. Structural characterization of Ru@CoSe biocatalyst with amorphous nanolayer. (a) Schematic illustration of the structures of CoSe and Ru@CoSe. (b) HAADF-STEM image of a single Ru@CoSe particle (blue: amorphous Ru@CoSe nanolayer). (c and d) HAADF-STEM images of atomic arrangement at the Ru@CoSe crystalline regions. (e) FFT pattern and (f) simulated crystal structure model of the Ru@CoSe crystalline regions (blue, Co atom; green, Se atom). (g) HAADF-STEM image of atomic arrangement at the Ru@CoSe amorphous layer. (h) Pseudocolour surface plot of a randomly selected area in (g) that shows the Ru atoms with various contrasts in the CoSe matrix. (i) High-resolution HAADF-STEM image of the amorphous Ru@CoSe nanolayer; the Ru atoms are marked by yellow circles. (j) Corresponding intensity profiles obtained from the area highlighted with white rectangles in regions 1−3 in (i). (k) STEM spectrum imaging of the amorphous nanolayer at the edge part of Ru@CoSe to show the distribution of Co, Se, and Ru elements.

number of patients unable to receive adequate and effective treatments. The inefficient healing of diabetic ulcers has been widely attributed to the high-ROS-level microenvironments, oxidative-stress effects, and inflammatory responses in chronic wounds, leading to the poor proliferation and differentiation of stem cells and also deterioration of many other functional cells.[7,13−15] Therefore, developing ROS-elimination materials to alleviate oxidative stress and relieve the inflammatory environments has provided opportunities to promote inflammatory and refractory wound healing, which include antioxidant nanostructures (catechol-based polymers,[16] carbon nanomaterials,[17] small-molecules-based reductants,[18,19] *etc.*) and antioxidase-like catalytic ROS-scavenging materials.[20−25]

In recent years, given the enormous benefits of antioxidase-like biocatalysts, such as efficient biocatalytic activity to preserve redox balance, low antigenicity, high stability after administration, and large-scale production,[26,27] there has been dramatically increased interest in designing biocatalysts *via* diverse transition metal compounds and metal nanoparticles that can mimic the function of natural antioxidases, including

https://doi.org/10.1021/acsnano.2c11448
ACS Nano 2023, 17, 2943−2957

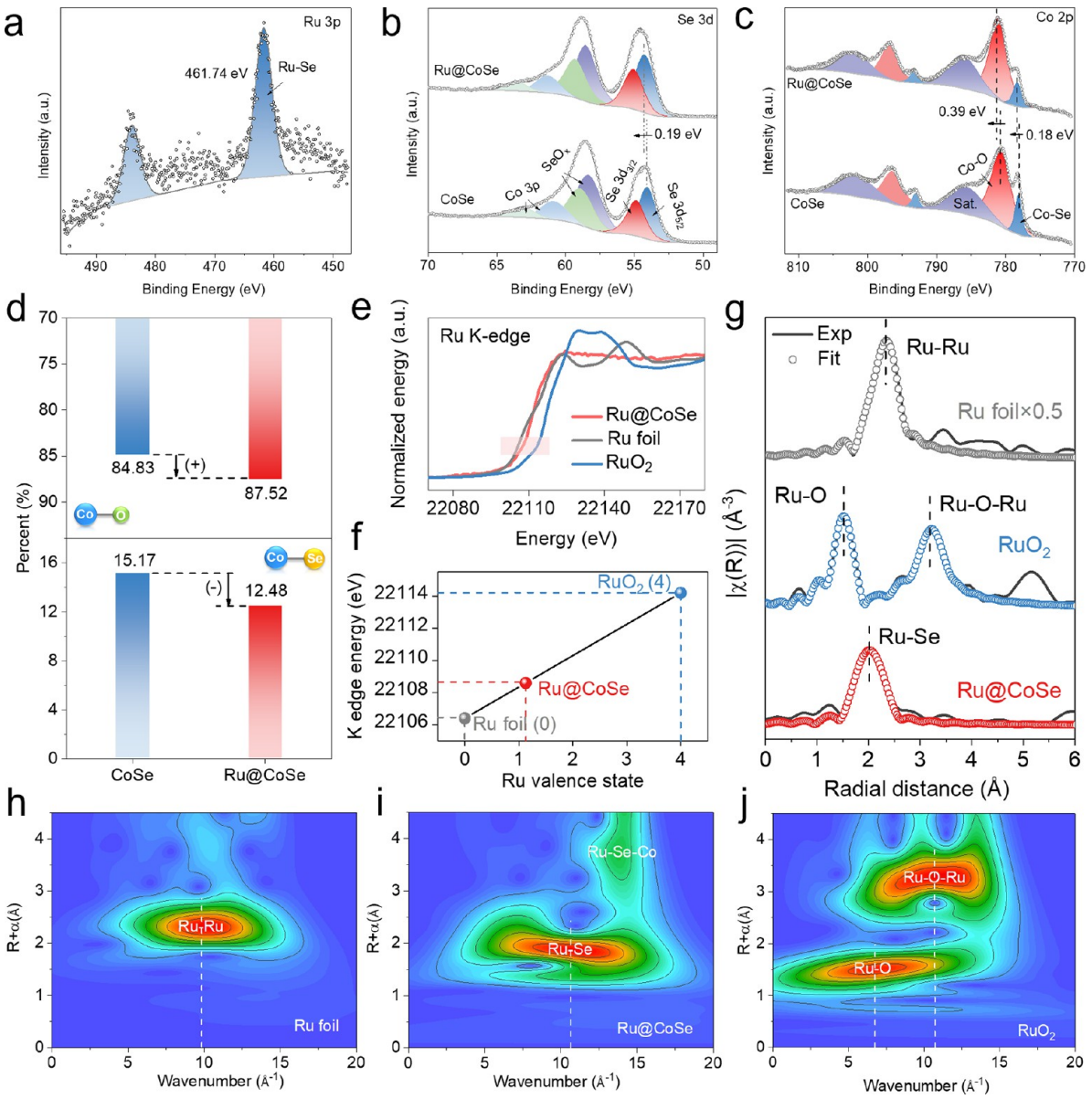

Figure 2. Chemical and electronic structures analysis of Ru@CoSe. (a–c) XPS spectra of the biocatalysts taken at (a) Ru 3p, (b) Se 3d, and (c) Co 2p regions. (d) Proportion of Co–Se and Co–O in CoSe and Ru@CoSe, which were obtained from XPS spectra at Co 2p regions. (e) XANES spectra of Ru *K*-edge over Ru@CoSe, Ru foil, and RuO_2. (f) Average valence states of Ru@CoSe, Ru foil, and RuO_2. (g) Fourier-transformed k^2-weighted $\chi(k)$-function of the EXAFS R space spectra and the fitting curves of Ru@CoSe, Ru foil, and RuO_2. (h–j) WT for the k^2-weighted Ru *K*-edge EXAFS signals.

catalase (CAT), glutathione peroxidase (GPx), and superoxide dismutase (SOD).[28−33] Despite thrilling progress in discovering catalytic ROS-scavenging materials,[26,27] the development of ultrafast and broad-spectrum antioxidase-like catalytic structures is still a grand challenge. They are mostly based on metal compounds, such as Co_3O_4,[34] MnO_2,[35] CeO_2,[36,37] and Pt-doped CeO_2,[38] due to their high biodegradability and good biocompatibility. Although these materials have shown good potential in protecting functional cells or combating oxidative stress-related diseases, they have rather poor catalytic efficiencies compared with natural antioxidases; thus, high dosages of nanomedicines are usually required.[18,27,29]

The ROS catalytic process of H_2O_2 or oxygen radicals involves multielectron reactions, complex intermediate bond formation, and high energy consumption in the final desorption of oxygen species.[39,40] The natural antioxidases can modulate these complex redox reactions *via* their axial coordination structures and 3D spatial configurations.[41,42] However, the currently established metal compounds-based antioxidase-like biocatalysts can hardly mimic this complex biochemical process. Notably, it has been found that the poor ROS catalytic activity of these metal compounds should be attributed to their deteriorated reversible redox properties of metal centers that originate from the coordinated electronegative atoms.[22,31] Thus, searching for a suitable strategy to overcome the unbalanced multielectron reactions and realize reversible catalytic cycles with ultrafast kinetics is essential. Among various metal compounds, transition metal selenides have become important catalytic materials to substitute the current metal oxides for diverse catalytic reactions due to their higher metallicity and tunable bandgap, atom environments, and electronic structures.[43] However, pristine metal selenides

https://doi.org/10.1021/acsnano.2c11448
ACS Nano 2023, 17, 2943−2957

also suffer from some inherent drawbacks for catalytic ROS scavenging, such as low catalytic activity and poor broad-spectrum scavenging ability. Therefore, it is crucial to develop an efficient strategy to adjust the catalytic atoms and bond microenvironments of metal selenides to obtain multifaceted and highly efficient ROS-scavenging abilities. However, this issue remains a major challenge that has been barely explored.

Here, in this study, to overcome the unbalanced multi-electron reactions in ROS biocatalysis, we report a cobalt selenide-based biocatalyst with amorphous Ru@CoSe nanolayer for ultrafast and broad-spectrum catalytic ROS-elimination. Owing to the enriched electrons and more unoccupied orbitals of Ru atoms, the amorphous Ru@CoSe nanolayer-equipped biocatalyst presents excellent catalytic scavenging activities toward H_2O_2, $\cdot O_2^-$, and DPPH·. Notably, the Ru@CoSe displays superior CAT-like reaction kinetics (V_{max}, 23.05 μM s^{-1}; turnover number (TON), 2.00 s^{-1}), indicating an ultrafast and efficient activity among all reported metal compounds-based biocatalysts. The mechanism understanding of the corresponding CAT-like catalytic process is also systematically investigated *via* the density functional theory (DFT), and the role of Ru atoms in modulating the electronic structure and reversible redox properties of active sites is also proposed. Systematic cellular studies demonstrate that the Ru@CoSe can efficiently rescue human mesenchymal stem cells (hMSCs) proliferation and preserve their angiogenic potential in the oxidative stress environment. *In vivo* experiments disclose that the Ru@CoSe displays superior ROS-elimination ability on the inflammatory diabetic wound.

RESULTS AND DISCUSSION

Synthesis and Structural Characterization of Ru@CoSe Biocatalyst with Amorphous Nanolayer. The Ru@CoSe material with an amorphous biocatalytic nanolayer is synthesized by a solvent-coordinated molecular template method, shown in Figure S1 and the Supporting Information.[44] By directly changing the Ru/Co molar ratio, a series of Ru-doped CoSe nanoparticles (NPs) are synthesized and named as Ru_x@CoSe (x = 1/5, 1/10, 1/20, 1/30, and 1/40) according to the Ru contents (see the Methods section for details). The scanning electron microscopy (SEM) images reveal that Ru_x@CoSe materials display granular morphology at the nanoscale (Figure S2). The powder X-ray diffraction (PXRD) patterns of Ru_x@CoSe display a similar crystal structure to that of CoSe (PDF#97-005-3959), revealing that the introduction of the Ru atom does not change the CoSe crystal phase or form a crystalline segregated biphases (Figure S3). Our subsequent tests on enzyme-mimetic properties confirm the higher optimized performance of $Ru_{1/10}$@CoSe NPs (Figure S4). Therefore, in the following, Ru@CoSe refers to $Ru_{1/10}$@CoSe unless otherwise stated.

Figure 1a illustrates the formation mechanism of the amorphous biocatalytic nanolayer of Ru@CoSe, which can be conjectured from the following structural characterization methods. First, the granular morphology and crystal structure of Ru@CoSe are verified by high-resolution transmission electron microscopy (HRTEM) images. In the HRTEM images, we observe the clear lattice fringes spacing of the (101) crystal plane of CoSe and no trace of Ru-related phases, which is consistent with the PXRD pattern (Figure S3). Then, the high-angle annular dark-field scanning transmission electron microscopy (HAADF-STEM) images depict the atomic-resolution structure of Ru@CoSe. As shown in Figure 1b, the crystalline regions of Ru@CoSe are surrounded by amorphous nanolayers (blue color), which are also presented in the HRTEM images (Figure S5). The atomic-resolution STEM images of Ru@CoSe nanocrystalline regions (Figure 1c-f) show a regular and bright CoSe atomic array. The corresponding fast Fourier transform (FFT) pattern of Ru@CoSe identifies the exposed (002) and (110) planes of CoSe along the $[\bar{1}10]$ zone axis (Figure 1e), which further suggests that Co and Se atoms are arranged with a hexagonal structure (Figure 1f). The atomic-resolution STEM images of the Ru@CoSe amorphous nanolayers are recorded to achieve more information about its structure (Figure 1g–i). Bright atoms are randomly distributed in the amorphous nanolayers, which can be recognized as Ru atoms placed on the surface. Subsequently, the line profiles for the HAADF image (Figure 1j) demonstrate the change in the atomic column intensity. This indicates that the presence of Ru atoms will lead to mismatching the CoSe crystalline structure. The selected-area energy-dispersive X-ray spectroscopy (EDX) elemental mapping (Figure 1k) further confirms that Ru atoms are uniformly distributed in the amorphous Ru@CoSe nanolayer. To sum up, introducing Ru species brings disorder and amorphization in the Ru@CoSe biocatalytic nanolayer that contains atomic Ru on the surface of the Ru@CoSe crystal.

X-ray photoelectron spectroscopy (XPS) was further conducted to gain insight into the chemical and electronic structures of Ru@CoSe biocatalysts. As shown in Figure 2a–c and Figure S7, Ru, Co, and Se signals are clearly detected, indicating the successful doping of Ru atoms into the CoSe matrix. The Ru $3p_{3/2}$ orbital of Ru@CoSe is located at 461.74 eV, confirming that Ru atoms with partial positive charges may exist in the form of Ru–Se bonds (Figure 2a).[45−47] Both the Se 3d and Co 2p peaks of Ru@CoSe show positive energy shifts in comparison with bare CoSe, which is ascribed to the increased electron density due to doping by Ru atoms (Figure 2b,c).[48] The high-resolution Co 2p spectrum of Ru@CoSe shows a decreased intensity of the surface selenization peak compared to the CoSe (Figure 2c). The fitted ratios of Co–O to Co–Se contents of Ru@CoSe (7.01) are higher than that of pristine CoSe (5.59), implying the high oxidation state of Co in Ru@CoSe.[49,50] Moreover, the Raman spectra further verify the electron transfer between Ru atoms and the CoSe substrate (Figure S8).[51]

Furthermore, to investigate the local coordination structure of Ru@CoSe biocatalysts, X-ray absorption spectroscopy (XAS) is performed. The normalized X-ray absorption near-edge structure (XANES) spectra of Ru *K*-edge present that the pre-edge peak of Ru@CoSe is located between Ru foil and RuO_2, indicating that Ru species in the biocatalyst carry a partially positive charge (Figure 2e). The corresponding valence state analysis indicates that Ru@CoSe is obviously a positive valence state of Ru foil (≈1.1, Figure 2f), which is consistent with XPS results. The k^2-weighted Fourier-transformed extended X-ray absorption fine structure spectra (FT-EXAFS) curves and corresponding fitting parameters of Ru@CoSe display a bond distance of 2.44 Å, which is attributed to the first-shell Ru–Se bond;[48,52] meantime, no obvious peaks of Ru–Ru (2.67 Å) or Ru–O–Ru bonds (3.17 or 3.57 Å) are observed, which strongly confirming only atomically dispersed Ru atoms in the Ru@CoSe (Figure 2g and Figure S9 and Table S1). Moreover, we perform the wavelet transform (WT) images to visually analyze the dispersed form of Ru species in the Ru@CoSe. As shown in Figure 2h–j, compared with Ru

https://doi.org/10.1021/acsnano.2c11448
ACS Nano 2023, 17, 2943−2957

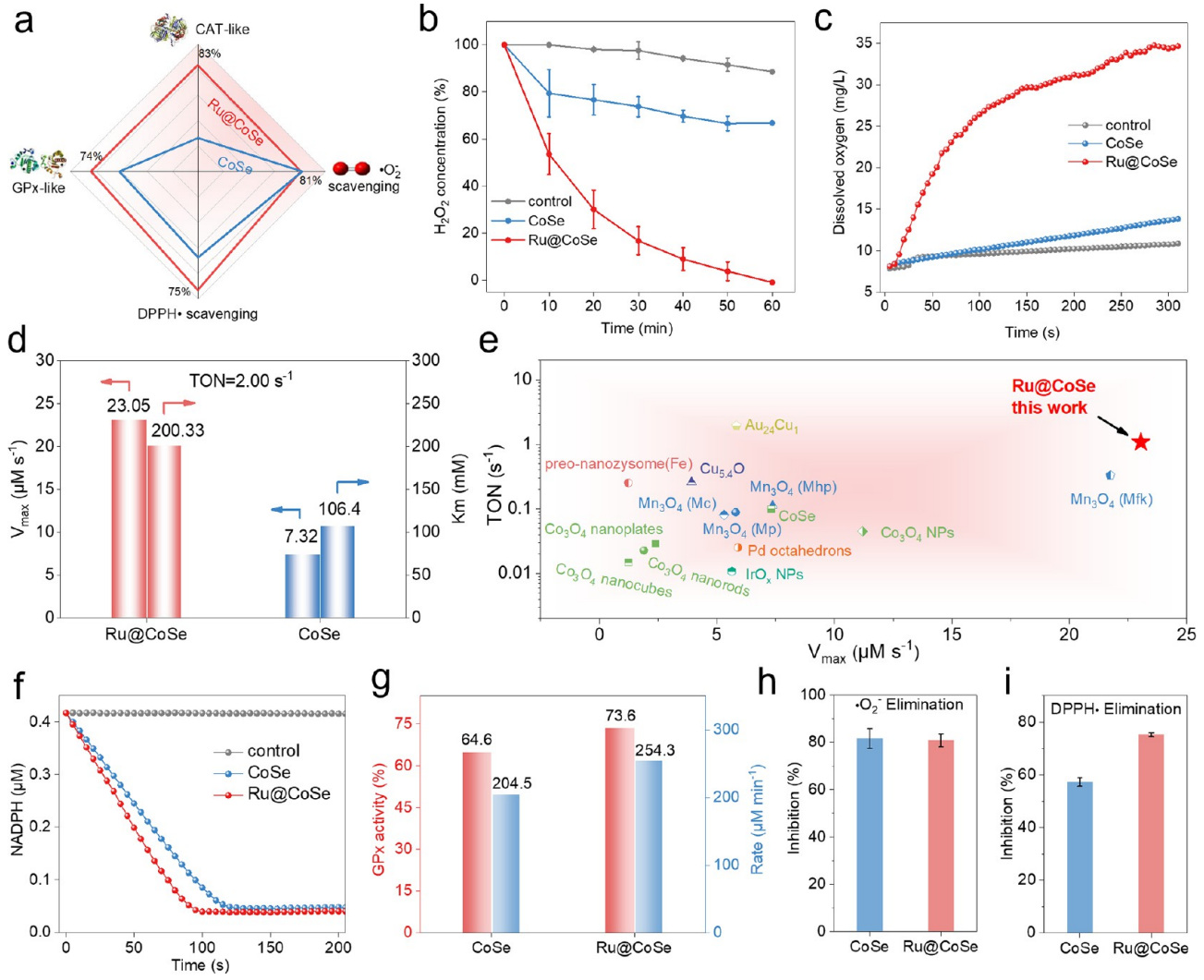

Figure 3. Biocatalytic ROS-elimination properties of CoSe and Ru@CoSe. (a) Radar map of biocatalytic ROS-elimination properties. CAT-like activities of CoSe and Ru@CoSe for (b) H_2O_2 elimination and (c) O_2 generation. (d) V_{max} and K_m values of biocatalysts for CAT-like activity to H_2O_2. (e) Comparison of the TON and V_{max} values of as-prepared biocatalysts with other currently established biocatalysts. The literature is shown in Table S2. (f) GPx-like activities and (g) corresponding consumption rate of NADPH. (h) $\cdot O_2^-$ and (i) DPPH· scavenging activities. In b, h, and i, n = 3 independent experiments; data are presented as mean ± SD.

foil and RuO_2, the Ru@CoSe exhibits a significant intensity maximum at ≈10.6 $Å^{-1}$, which is assigned to Ru−Se coordination. Thus, the consistent STEM, XPS, and XAS data confirm that the Ru species are atomically dispersed in the amorphous Ru@CoSe nanolayer and Ru is uniformly coordinated by Se.

Evaluation of ROS-Elimination Activities. After validating the chemical and electronic structures of Ru@CoSe, the biocatalytic ROS elimination properties and the influence of the surface amorphous Ru@CoSe nanolayer are then systematically investigated. The general catalytic profiles of biocatalysts (CoSe and Ru@CoSe) are shown in Figure 3a. To pinpoint the detailed catalytic performances of these biocatalysts, we first examined the CAT-like activities of CoSe and Ru@CoSe. The H_2O_2 removal efficiency of CoSe is 16.6% (30 min), whereas the Ru@CoSe gives rise to a 5.03-fold increase to 83.6%, and a complete elimination in 60 min (Figure 3b). Simultaneously, the O_2 generation tests verify that Ru@CoSe biocatalyst can efficiently decompose H_2O_2 substrate to produce massive O_2 (Figure 3c), suggesting the efficient CAT-like activity of Ru@CoSe. Moreover, Ru@CoSe presents a dose-dependent H_2O_2 removal and O_2 generation (Figure S10). Then, we calculate the values of Michaelis constant (K_m), maximal reaction velocity (V_{max}), and turnover number (TON) to reveal the steady-state catalytic kinetics. Compared with CoSe, the Ru@CoSe displays larger V_{max} (23.05 $\mu M\ s^{-1}$) and higher TON (2.00 s^{-1}), indicating that Ru@CoSe possesses more efficient CAT-like catalytic kinetics toward H_2O_2 (Figure 3d and Figure S11). Subsequently, we compare the V_{max} and TON values of Ru@CoSe with currently established transition metal-based ROS-scavenging materials, including RuTe,[53] Co_3O_4,[34] $Cu_{5.4}O$,[54] $Au_{24}Cu_1$,[40] *etc.*, (Figure 3e and Table S2), indicating the optimized CAT-like activity of Ru@CoSe among these established biocatalysts.

Besides the CAT-like catalytic performance, we then carefully study the influence of the surface amorphous Ru@CoSe nanolayer on the other enzyme-mimetic properties (GPx and SOD) and other kinds of radicals (reactive nitrogen species, RNS). The GSH-dependent GPx is crucial for maintaining cellular homeostasis, which can decompose H_2O_2 into H_2O with the participation of GSH. The GPx-like catalytic activity can be monitored by the glutathione reductase

https://doi.org/10.1021/acsnano.2c11448
ACS Nano 2023, 17, 2943−2957

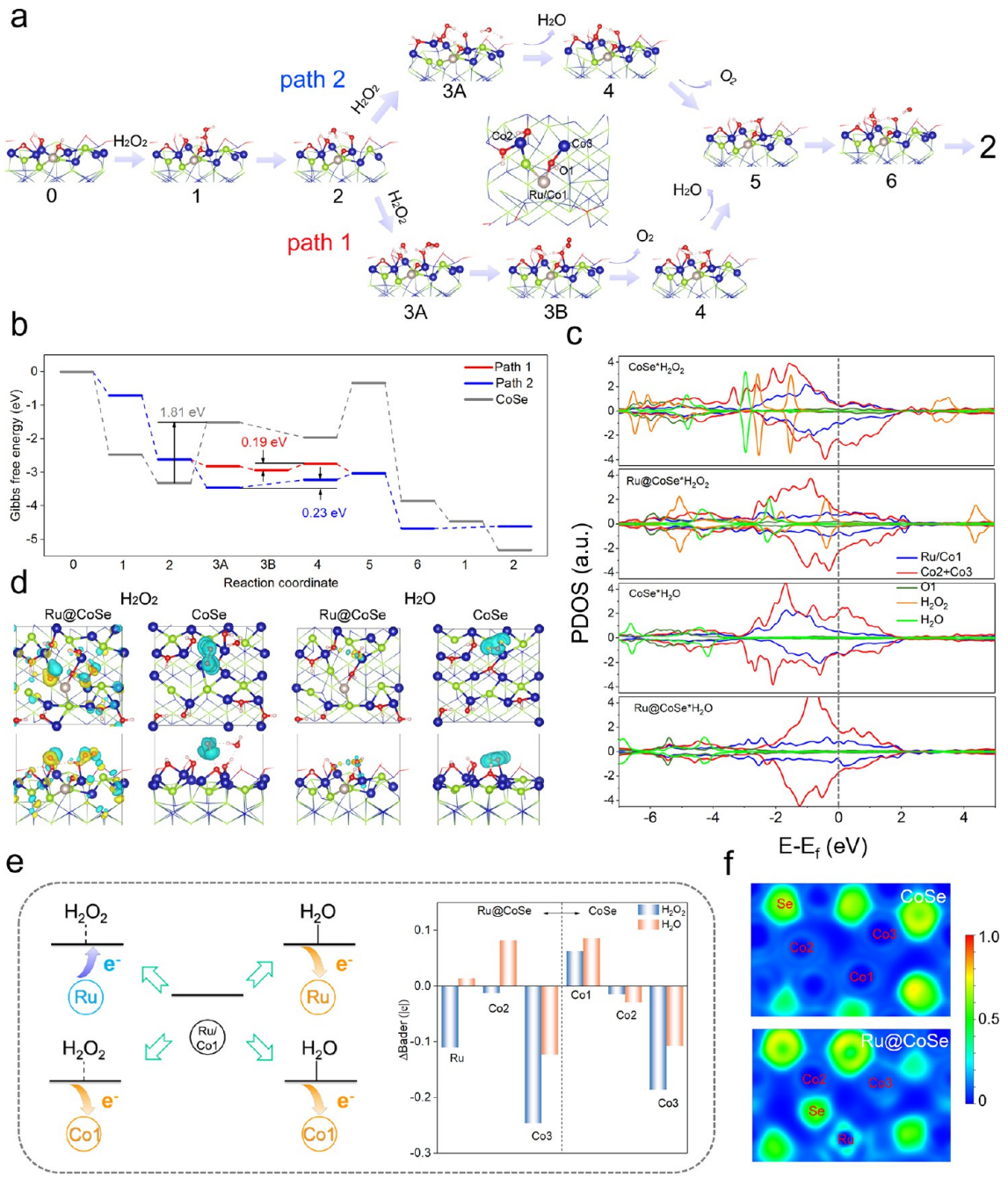

Figure 4. Theoretical calculations on the detailed mechanisms and catalytic pathways. (a) Optimized structures of intermediates along the pathway on Ru@CoSe. The green, blue, silver, red, and pink balls represent Se, Co, Ru, O, and H atoms, respectively; atom labels are shown in the upper right corner in the top view, and some atoms are simplified as lines. (b) Free energy profiles for H_2O_2 decomposition on the Ru@CoSe (paths 1 and 2) and CoSe. (c) PDOS for structure paths 1−3A, CoSe-3, paths 1−5, and CoSe-5 from up to bottom. (d) Charge density differences for paths 1−3A, CoSe-3, paths 1−5, and CoSe-5 from left to right. The isosurface level is 0.1 (0.01 for paths 1−5). yellow, charge accumulation; blue, charge depletion. (e) Left, charge transfer schematic images of adsorption structures for H_2O_2 and H_2O; right, Bader charge difference between the adsorption structures of H_2O_2 and H_2O and the slab. The positive represents electron injection, while the negative represents electron depletion. (f) ELF of structure 3A of paths 1−3A and CoSe-3.

coupled assay and the decrease of NADPH concentration. As shown in Figure 3f,g, though both Ru@CoSe and CoSe show strong GPx-like activity, Ru@CoSe displays an increased reaction rate of 254.3 μM min^{-1}, which is higher than that of CoSe (204.5 μM min^{-1}). Additionally, the Ru@CoSe shows dose-dependent GPx-like catalytic activity (Figure S12). This result is amazing because metals are generally thought to have poor GPx-like activity,[40] it is expected that the high GPx-like activities of CoSe and Ru@CoSe can be exploited to remove lipid peroxides and oxidative damage.

The SOD is also important in the anti-ROS systems *via* catalytic scavenging of $\cdot O_2^-$. Here, $\cdot O_2^-$ free radical scavenging is investigated by the nitrotetrazolium blue chloride method. Interestingly, both the CoSe and Ru@CoSe exhibit significant $\cdot O_2^-$ scavenging efficiency (~80% within 5 min (Figure 3h)), indicating that the amorphous Ru@CoSe nanolayer offers no

https://doi.org/10.1021/acsnano.2c11448
ACS Nano 2023, 17, 2943−2957

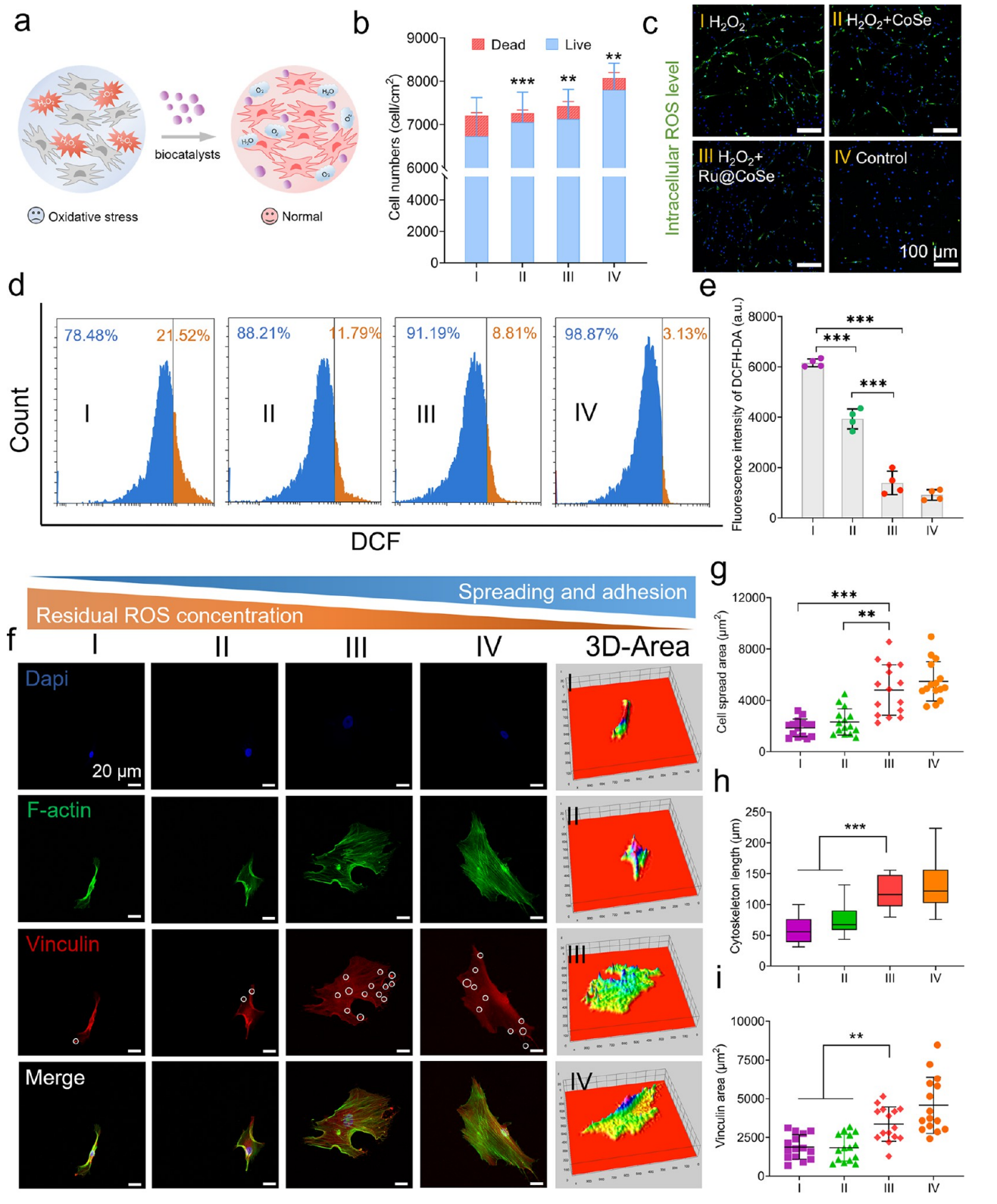

Figure 5. Stem cells protection from ROS attack *via* Ru@CoSe biocatalysts. (a) Schematic illustration of Ru@CoSe for alleviating oxidative stress. (b) Live/Dead cell numbers; image data are shown in Figure S18, data are presented as mean ± SD, $n = 4$. (c) Fluorescence images of DCFH-DA staining. (d) Flow cytometry data and (e) quantitative analysis of cells after DCFH-DA staining with biocatalysts from c (data are presented as mean ± SD, $n = 4$). (f) F-actin and Vinculin staining of hMSCs after different treatments. (g) Spreading area, (h) cytoskeleton length, and (i) adherent spot area analysis of each group on F-actin/Vinculin staining. In g–i, $n = 15$, all values are presented as mean ± SD *p*-values are assessed by one-way analysis; $^*P < 0.05$, $^{**}P < 0.01$, and $^{***}P < 0.001$. Group I, H_2O_2; group II, H_2O_2+CoSe; group III, H_2O_2+Ru@CoSe; group IV, control. The control group is hMSCs cultured in normal media without adding H_2O_2; the other groups are cultured in media containing 100 μM H_2O_2.

https://doi.org/10.1021/acsnano.2c11448
ACS Nano 2023, 17, 2943−2957

change to the SOD-like catalytic activity. DPPH· is a common reagent to evaluate the ability of biocatalysts to remove RNS. As shown in Figure 3i and Figure S13, Ru@CoSe presents an excellent and dose-dependent effect in the removal of DPPH· radical, which is obviously higher than that of the CoSe. Taken together, we have disclosed that the Ru@CoSe biocatalyst presents a much-enhanced CAT-like catalytic activity than the pristine CoSe. The introduction of atomic Ru also improves the GPx-like activity and RNS scavenging ratio.

Theoretical Calculation of Catalytic CAT-Like Pathways. To elucidate the detailed mechanisms and differences between the catalytic activity Ru@CoSe and CoSe, we conduct systematic density functional theory (DFT) calculations to simulate the H_2O_2-elimination and O_2-generation processes. The optimized biocatalyst's structure (CoSe and Ru@CoSe) is shown in Figure S14. With the introduction of Ru atoms, it is interesting to find out that the crystalline surface of CoSe becomes amorphous after full relaxation, which is consistent with our HRTEM and STEM imaging results. Since H_2O_2 is easily decomposed into OH* by biocatalysts, we construct a partially hydroxylated structure to explore subsequent catalytic pathways (Figure S15).

Parts a and b of Figure 4 show the critical intermediate structures and Gibbs free energy diagrams along the optimized reaction paths during the H_2O_2 decomposition on both Ru@CoSe and CoSe. In response to the amorphous structure of Ru@CoSe, we propose two potential paths for H_2O_2 decomposition on the Ru@CoSe. For path 1, a second H_2O_2 molecule adsorbs on the near-surface and reacts with catalysts *via* hydroxyl; the rate-determining step is the release of O_2 (structure 3B to 4, 0.12 eV). Conversely, for path 2, a second H_2O_2 molecule interacts with the Co site to become OOH*, then followed by two uphill steps with energy gaps of 0.23 eV (release of H_2O) and 0.19 eV (release of O_2), respectively. However, for the CoSe, the reaction pathway is similar to path 2, with a very high energy gap of 1.81 eV (Figure S16). Meanwhile, the adsorptions of H_2O_2, OOH*, and H_2O* (CoSe 3, 4, and 5) all show obviously higher energies than Ru@CoSe.

The key to a high CAT-like activity is an appropriate interaction strength between the active sites and reaction intermediates. To demonstrate the role of the Ru atoms in modulating the interaction of adsorbates with the active sites, the projected density of states (PDOS, Figure 4c) and charge density differences (Figure 4d) of important adsorbates (H_2O_2 and H_2O) on biocatalysts are calculated. It is found that the interaction of H_2O_2 with the Ru@CoSe surface is stronger than CoSe (1.5 eV), and both of the surfaces weakly interact with H_2O, indicating that the Ru@CoSe surface is favorable for the adsorption of H_2O_2 and the removal of H_2O, thereby accelerating the H_2O_2-decomposition process. Moreover, different from the adjustment of the electronic structure for the adsorbed molecules on the CoSe surface, an electronic rearrangement, involving a lot of surfaces, subsurface atoms, and the hydroxyls, is observed on the surface of Ru@CoSe after H_2O_2 adsorption. Meanwhile, only relatively weak hydrogen bonds exist in the adsorption of H_2O, which further confirms the strong interaction between H_2O_2 and Ru@CoSe.

We then calculate the Bader charge difference between the adsorption structures and the slab surface for active sites (Ru/Co1, Co2, and Co3 atoms) to further clarify the role of Ru atoms for H_2O_2 decomposition. As shown in Figure 4e, the charge transfer direction of Ru/Co1 sites is different for the H_2O_2 adsorption; the electron flows out from Ru sites at about 0.110 |e| but injects into Co1 sites at about 0.063 |e|. Conversely, for H_2O adsorption, the charge transfer of Ru sites changes direction to a positive value of 0.014 |e| and that of Co1 sites is 0.086 |e| (Figure 4e). More interestingly, in contrast to CoSe, the charge transfer direction changes for Co2 sites in Ru@CoSe under different adsorbates. It seems that Ru atoms act as "regulators" to tune the electronic state of the Co sites during the catalytic process. The electron localization function (ELF) of H_2O_2 adsorbed configurations further confirmed the above conclusion. The green color with a value of 0.5 corresponds to the electron-gas-like pair probability as in metallic bonds. As shown in Figure 4f, the Ru@CoSe shows more electron-gas-like around Ru atoms, meaning a better charge transfer feature.

Stem Cells Protection and Fates Regulation. After revealing the efficient catalytic ROS-scavenging abilities of Ru@CoSe biocatalyst, we then carefully examine their biomedical application potentials in protecting stem cells in high ROS-level microenvironments and regulating inflammatory diabetic wound healing (Figure 5a). For stem cell protection, first, we examine the biocompatibility of the biocatalysts (Ru@CoSe and CoSe) on hMSCs in a simulated ROS environment (100 μM H_2O_2). As shown in Figure S17, the biocatalysts exhibit no noticeable cytotoxicity and a very slow degradation rate. Meanwhile, the Live/Dead staining shows nearly no dead cells in the biocatalysts' group (Figure S18). The corresponding quantitative analysis indicates that the biocatalysts can enhance the survival of hMSCs in the ROS environment, demonstrating acceptable biocompatibility of both Ru@CoSe and CoSe (Figure 5b). Subsequently, we employ the 2,7-dichlorofluorescein diacetate (DCFH-DA) probe to quantify the intracellular ROS removal efficiency of hMSCs by the biocatalysts. As shown in Figure 5c, an obvious ROS signal (green) is observed in group I (100 μM H_2O_2). However, the ROS signal is significantly reduced after treatment with biocatalysts, especially in the case of Ru@CoSe. This result indicates that Ru@CoSe effectively scavenges intracellular ROS. Moreover, the quantitative analysis reveals that the Ru@CoSe group exhibits a weak ROS signal, which is comparable to the control group (Figure 5d,e). The above results demonstrate that Ru@CoSe has an efficient ROS scavenging ability, which can be used to regulate stem cell fates under high ROS-level conditions.

It has been reported that ROS will not only lead to cell apoptosis but also affects the arrangement of the cytoskeleton and the expression of adhesion proteins, thereby inhibiting cell motility, proliferation, and differentiation.[55,56] Therefore, we further evaluate its effect on the spreading and adhesion of hMSCs. As shown in Figure 5f, H_2O_2-treated hMSCs (group I) show abnormal spreading and morphology with few skeletal tissues and protrusions. By contrast, the Ru@CoSe-incubated hMSCs present outspread and flattened morphology with a well-organized cytoskeleton. The quantitative analysis of cell spreading area and cytoskeleton length on the F-actin staining also demonstrates a larger spreading area and higher aspect ratio for Ru@CoSe-incubated hMSCs than group I, which is equivalent to the control group (Figure 5g,h). Additionally, to evaluate the variation in the spreading area, we investigate the focal adhesion (FA) structures that influence cell migration and spreading, which are key elements linking the actin cytoskeleton and the extracellular matrix.[57,58] As shown in Figure 5f, H_2O_2-treated hMSCs show decreased vinculin

https://doi.org/10.1021/acsnano.2c11448
ACS Nano 2023, 17, 2943−2957

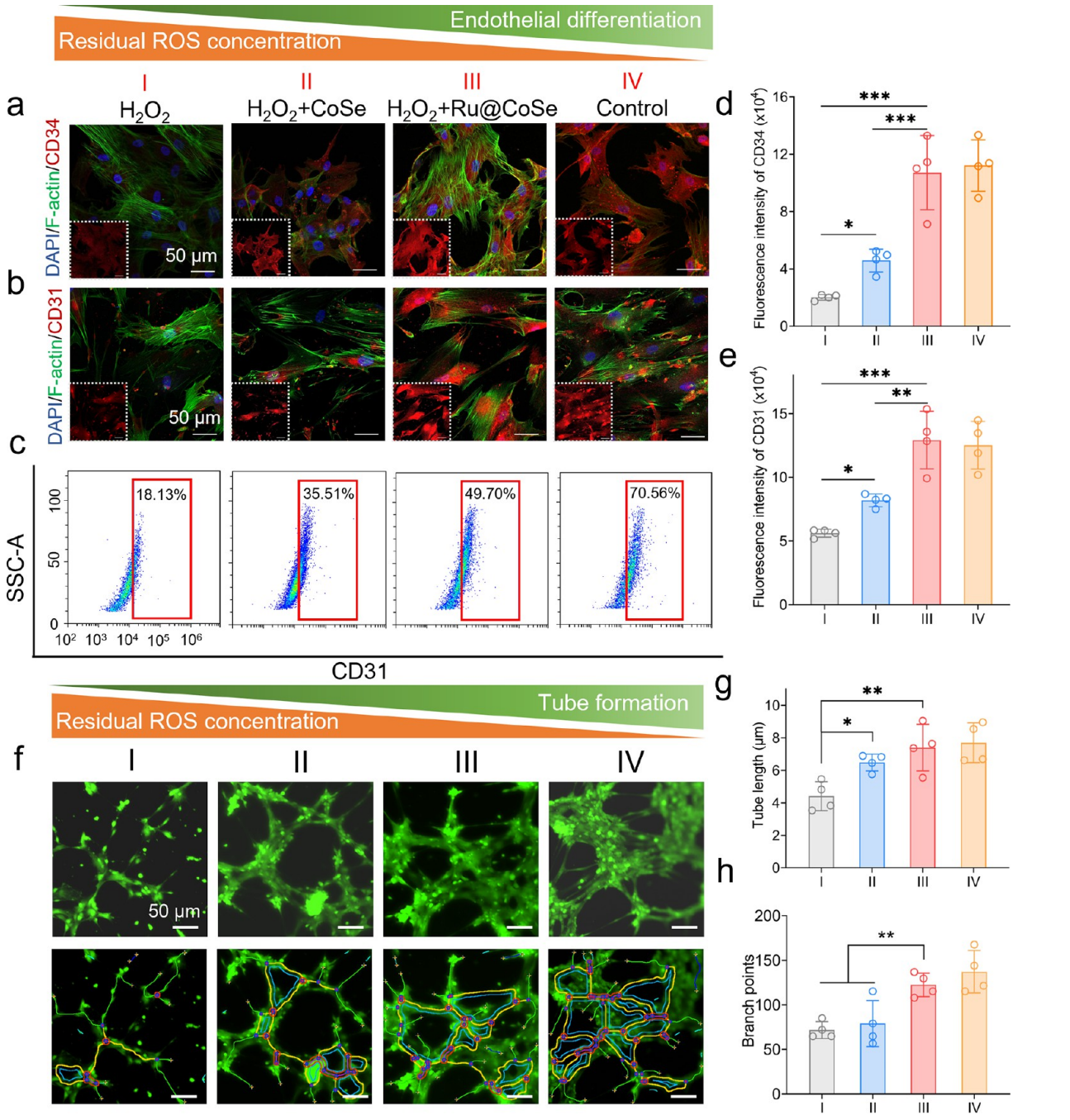

Figure 6. Endothelial differentiation potential of hMSCs in high ROS level media. Staining of endothelial cells' specific markers: (a) CD34/F-actin staining and (b) CD31/F-actin staining. (c) Flow cytometric analysis of CD31. Quantitative analysis of cells after (d) CD34 and (e) CD31 staining. (f) Representative images of the ability of tube formation for differentiated hMSCs. Statistical analysis of (g) capillary length and (h) branch points. All values are expressed as mean ± SD, $n = 4$. p-values are assessed by one-way analysis; *$P < 0.05$, **$P < 0.01$, and ***$P < 0.001$. Group I, H_2O_2; group II, H_2O_2+CoSe; group III, H_2O_2+Ru@CoSe; group IV, control. The control group is hMSCs cultured in endothelial basal medium-2 without adding H_2O_2; the other groups are cultured in endothelial basal medium-2 containing 100 μM H_2O_2.

expression and are mainly distributed around the nucleus, indicating poor adhesion of hMSCs to the substrate under the high ROS environment. However, after coincubation with Ru@CoSe, the hMSCs present distinct, spatially distributed, and uniform expressions of FA, which indicates the enhanced adhesion between hMSCs and substrates. Moreover, further quantitative analysis also exhibits an increased adhesion area for Ru@CoSe-protected hMSCs than group I (Figure 5i). These results suggest that Ru@CoSe effectively reduces the damage of hMSCs, thereby achieving cytoskeleton remodeling and better cell adhesion.

Besides protecting the spreading and adhesion of hMSCs, we also verify the differentiation potential of hMSCs on vascular endothelial cells (ECs) in a high ROS environment. During the differentiation of hMSCs to ECs, CD31 and CD34 are considered the specific markers of ECs.[59] As shown in Figures S19 and S20, very limited signals for both CD31 and CD34 are obtained in pure hMSCs and H_2O_2-treated hMSCs, suggesting that the high ROS environment damages the

https://doi.org/10.1021/acsnano.2c11448
ACS Nano 2023, 17, 2943−2957

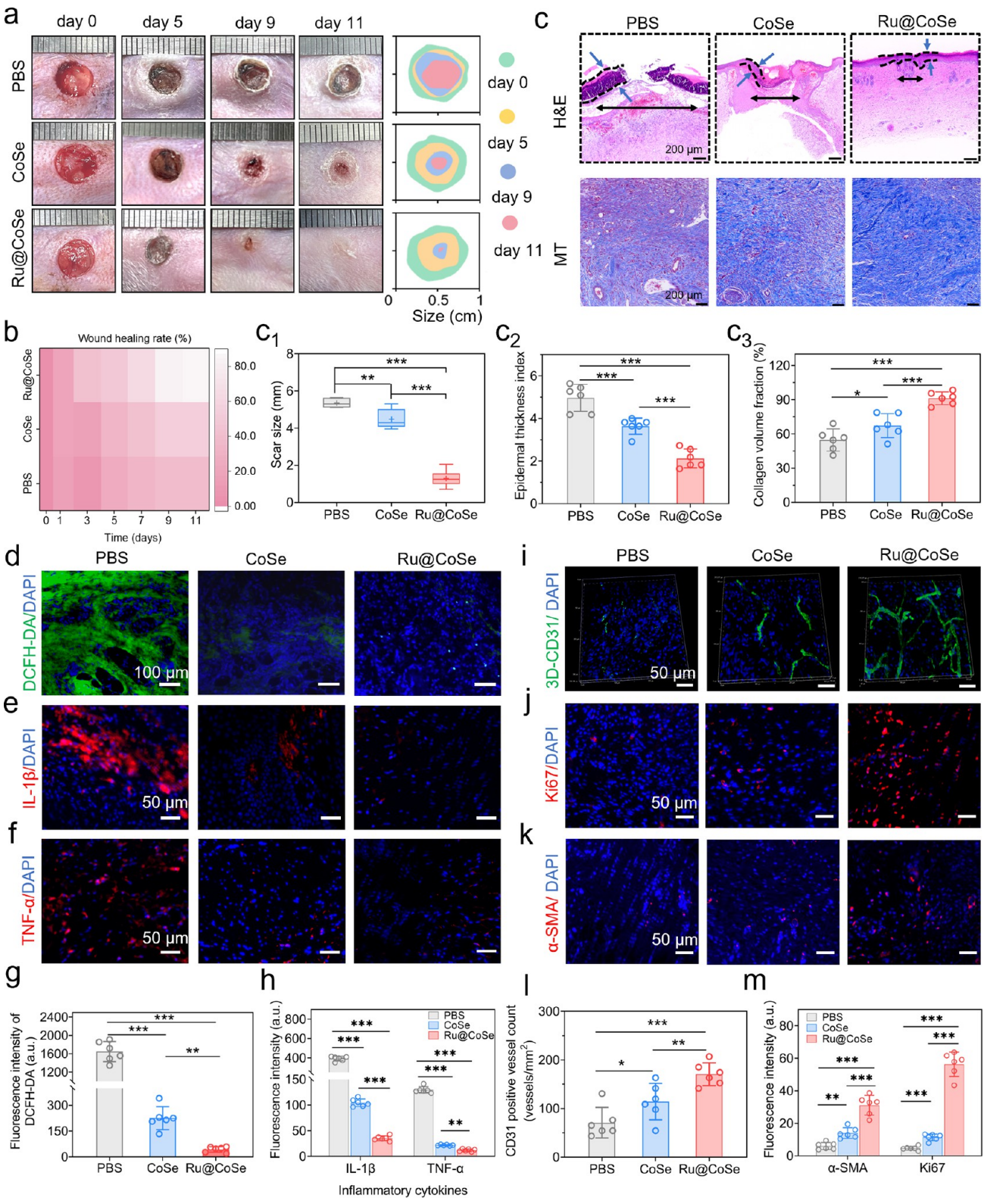

Figure 7. Treating effects of Ru@CoSe in promoting inflammatory diabetic wound healing. (a) Representative digital images of the diabetic wound area in response to different treatments on day 0, day 5, day 9, and day 11. (b) Time evolution of the wound sizes after different treatments. (c) H&E and Masson staining images of the epidermal tissue slices for each group on day 11. Quantification of the (c_1) scar size, (c_2) epidermal thickness index, and (c_3) collagen deposition in different groups. Fluorescence staining of (d) DCFH-DA, (e) IL-1β, and (f) TNF-α. (g and h) Immunofluorescence quantitative statistics of DCFH-DA, IL-1β, and TNF-α. (i) CD31/DAPI staining images of 3D reconstruction. (j) Ki67 and (k) α-SMA staining images of the epidermal histological sections in different groups on day 11. (l) Neovascularization count statistics according to (i). (j) Immunofluorescence quantitative statistics of Ki67 and a-SMA. All values are expressed as mean ± SD, $n = 6$. p-values are assessed by one-way analysis and marked as asteroids. *$P < 0.05$, **$P < 0.01$, and ***$P < 0.001$.

https://doi.org/10.1021/acsnano.2c11448
ACS Nano 2023, 17, 2943−2957

Scheme 1. Illustration of the Working Mechanisms of Ru@CoSe in Scavenging ROS, Protecting Stem Cells, and Promoting Angiogenesis and Diabetic Wound Healing

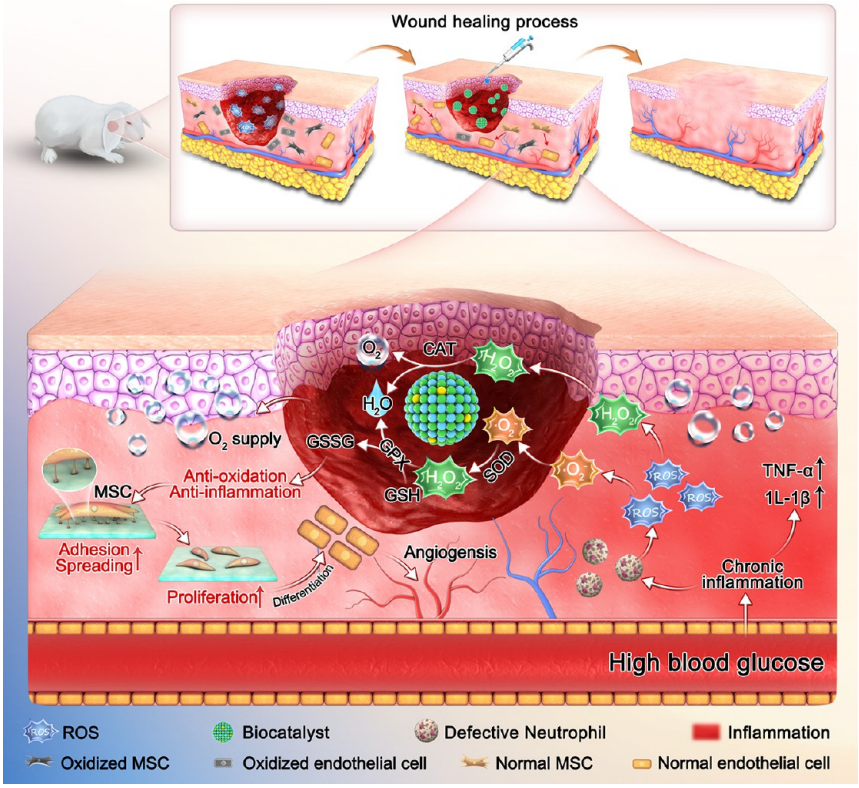

differentiation ability of hMSCs into ECs. However, for biocatalysts-incubated hMSCs, the enhanced red signals are observed in the whole well, especially Ru@CoSe, which shows similar results to the control group (Figure 6a,b). The corresponding quantitative analysis also confirms that the Ru@CoSe group exhibits a strong signal intensity, which is comparable to the control group, indicating that Ru@CoSe can effectively scavenge ROS and rescue the differentiation ability of hMSCs into ECs (Figure 6c–e). Moreover, to explore the angiogenesis ability of hMSCs after different treatments, the tube formation assay is carried out, which is used for simulating angiogenesis *in vitro*.[60] In principle, the higher the degree of endothelial differentiation of hMSCs, the more tubular networks will be formed. As shown in Figure 6f–h, the Ru@CoSe group presents higher efficiency than the H_2O_2 and CoSe groups in promoting tube formation, characterized by more visible tube-like structures, higher branch numbers, and longer capillary length. Overall, the above-mentioned results demonstrate that Ru@CoSe can maintain the angiogenic potential of hMSCs by alleviating the cellular function damage in the oxidative stress environment.

Treating Effects for Inflammatory Diabetic Wound Healing. After verifying the *in vitro* rescue ability of Ru@CoSe biocatalyst on the hMSCs' differentiation function, we further evaluate the *in vivo* performance of Ru@CoSe in promoting inflammatory diabetic wound healing. First, we establish a hyperglycemic rabbit ear ulcer model to assess angiogenesis, anti-inflammatory, and healing ability in diabetic wounds.[61] The photographs of the wound healing process and the wound healing rate are summarized in Figure 7a,b and Figure S21. The Ru@CoSe group exhibits a higher wound healing rate than the other groups and can be almost completely healed on day 11, while wounds treated by the CoSe or phosphate-buffered saline (PBS) group are still exposed and covered by eschar. Then, the histological status of the treated wound after 11 days is observed by the hematoxylin–eosin (H&E) and Masson trichrome staining on the wound tissues. As shown in Figure 7c,c_1–c_3 and Figures S22 and S23, a larger scar size and epidermal thickness index are presented in the damaged skin tissue, which is attributed to poor wound healing and impaired tissue remodeling caused by dramatically reduced collagen. On the 11th day, only a few loose and disordered collagen fibers appear in the CoSe or PBS group. In contrast, the Ru@CoSe-treated group shows a lower epidermal thickness index, more collagen deposition, and better-arranged, denser, and thicker collagen fibers in skin tissues, which is similar to normal skin and dermis. Thereafter, we take the DCFH-DA, dihydroethidium (DHE), interleukin-1beta (IL-1β), and tumor necrosis factor-α (TNF-α) staining to examine the alleviation of the oxidative stress and inflammation in the wound area by Ru@CoSe, the data are displayed in Figure 7d–h and Figure S24. The unhealed wound shows extensive areas with ROS (green) and inflammatory factor (red) signals; the Ru@CoSe group displays nearly no ROS and inflammatory factors, indicating an efficient ROS elimination ability in the inflammatory diabetic wound by the Ru@CoSe.

The wound-healing process is usually accompanied by the formation of new capillaries.[62] Thus, we take the CD31, Ki67, and α-smooth muscle actin (α-SMA) staining to study the cell proliferation and angiogenesis in the wound area. As shown in Figure 7i,l and Figure S25, the Ru@CoSe group exhibits higher CD31 expression and longer neovascular length than the PBS and CoSe groups. Likewise, the Ki67 expression in the Ru@

https://doi.org/10.1021/acsnano.2c11448
ACS Nano 2023, 17, 2943–2957

CoSe group is also obviously higher than the PBS and CoSe groups (Figure 7j), suggesting that the Ru@CoSe can promote cell proliferation during healing, thus accelerating granulation tissue formation and promoting collagen deposition. The timely activation of the angiogenic responses during wound healing is important for wound repair and is investigated by immunofluorescence staining of α-SMA. As shown in Figure 7k,m, the Ru@CoSe group shows the strongest fluorescence intensity among all groups, indicating an earlier or stronger angiogenic response for the Ru@CoSe-treated group than others at the wound healing stage. Moreover, the biosafety of biocatalysts is also evaluated by H&E staining of major organs (heart, liver, spleen, lung, and kidney); the data clearly show that there is no obvious damage and abnormality in the main organs and tissues, indicating the low cytotoxicity of our biocatalysts. Taken together, our data proves that Ru@CoSe can serve as an effective and safe nanomedicine to combat oxidative stress and achieve ultrafast inflammatory diabetic wound healing.

CONCLUSION

In summary, our data have confirmed that the as-prepared cobalt selenide-based biocatalyst with an amorphous Ru@CoSe nanolayer is an ideal and efficient antioxidase-like nanoplatform for ultrafast and broad-spectrum catalytic ROS-elimination. The structure merits and catalytic performances of the amorphous Ru@CoSe nanolayer with atomically dispersed Ru species have been systematically investigated for ROS elimination. Our experimental studies and theoretical calculations confirm that the as-prepared Ru@CoSe biocatalysts present excellent catalase-like reaction kinetics (V_{max}, 23.05 μM s^{-1}; TON, 2.00 s^{-1}) due to the enriched electrons and more unoccupied orbitals of Ru atoms. Ru species act as "regulators" that tune the electronic state of Co sites and modulate the interaction of oxygen intermediates, thus improving the reversible redox properties of catalytic sites and surpassing most of the currently reported metal compounds-based ROS biocatalysts. This study also highlighted that designing an amorphous biocatalytic nanolayer for ROS catalytic reactions might help maximize intrinsic activity, accessible activated surface, and atomic utilization efficiency.

In vitro and *in vivo* experiments also show that the Ru@CoSe significantly downregulates intracellular ROS concentration and alleviates hypoxia, thereby rescuing hMSCs proliferation, maintaining their angiogenic potential, ultimately promoting tissue regeneration and achieving ultrafast inflammatory diabetic ulcer wound healing (Scheme 1). We are convinced that this study offers an effective nanomedicine for catalytic ROS-scavenging and ultrafast healing of the inflammatory wound, which promotes the development of artificial biocatalysts to substitute nature antioxidases for anti-ROS therapies and chronic inflammatory diseases (Table S3).

METHODS

Ru@CoSe was prepared according to the procedures reported by another researcher.[44] Typically, 1 mmol of $CoCl_2{\cdot}6H_2O$ and 0.1 mmol of $RuCl_3{\cdot}xH_2O$ were dispersed into 60 mL of deionized water. One millimol of Na_2SeO_3 was added into the above solution under magnetic stirring. Then, 20 mL of DETA was slowly added into the above solution under magnetic stirring. Later, 1 mL of $N_2H_4{\cdot}H_2O$ was added to the mixture and stirred at room temperature for 30 min. Subsequently, the mixture was transferred into a Teflon-lined autoclave and maintained at 180 °C for 15 h. The final black products were obtained by centrifugation (10000 rpm, 6 min) and washed with absolute ethanol and distilled water, followed by drying at 60 °C in a vacuum oven. The synthesis of Ru_x@CoSe NPs with different Co/Ru molar ratios (5:1, 20:1, 30:1, and 40:1) was similar to that of $Ru_{1/10}$@CoSe NPs, except that the proportion of $RuCl_3{\cdot}xH_2O$ used has changed. According to the different molar ratios between $CoCl_2{\cdot}6H_2O$ and $RuCl_3{\cdot}xH_2O$ (5:1, 10:1, 20:1, 30:1, and 40:1), the obtained five samples are denoted as $Ru_{1/5}$@CoSe, $Ru_{1/10}$@CoSe, $Ru_{1/20}$@CoSe, $Ru_{1/30}$@CoSe, and $Ru_{1/40}$@CoSe, respectively. For comparison, the control samples, bare CoSe, have also been synthesized without Ru precursors under the same conditions. It is worth noting that the Ru@CoSe in the above sections refers to the best-performing $Ru_{1/10}$@CoSe unless specified otherwise.

ASSOCIATED CONTENT

Supporting Information

The Supporting Information is available free of charge at https://pubs.acs.org/doi/10.1021/acsnano.2c11448.

Discussions of materials and methods and experimental details, figures of schematic synthesis process, SEM images, XRD patterns, and enzyme-mimetic properties of Ru_x@CoSe, TEM images, HRTEM images, XPS survey spectra, and Raman spectra of CoSe NPs and Ru@CoSe NPs, EDS mapping images, EXAFS in k-space and corresponding fitting curves (dots), and ROS-elimination activities of Ru@CoSe, DFT's structural models of CoSe NPs and Ru@CoSe NPs, optimized structures of intermediates on CoSe NPs, hMSCs viability determined by CCK-8 assays, Live/Dead staining images, CD34 and CD31 staining images of hMSCs after treated by CoSe NPs and Ru@CoSe NPs, change of wound sizes, H&E staining images, Masson staining images, DHE staining images, CD31 immunohistochemical staining images, and corresponding 3D reconstruction maximum intensity projection (MaxIP) of wounds tissue slices, and H&E staining images of visceral tissue slices, and tables of EXAFS fitting parameters of Ru K-edge, comparison of the TON values of our synthesized catalysts with other reported biocatalysts, and earlier reported antioxidase-like biocatalysts for ROS elimination (PDF)

AUTHOR INFORMATION

Corresponding Authors

Wei Geng − *College of Polymer Science and Engineering, Med-X Center for Materials, State Key Laboratory of Polymer Materials Engineering, Sichuan University, Chengdu 610065, China;* orcid.org/0000-0002-6757-1102; Email: gengw15@163.com

Qiu Chen − *Department of Endocrinology, Hospital of Chengdu University of Traditional Chinese Medicine, Chengdu 610072, China;* orcid.org/0000-0003-1089-4194; Email: chenqiu1005@cdutcm.edu.cn

Chong Cheng − *College of Polymer Science and Engineering, Med-X Center for Materials, State Key Laboratory of Polymer Materials Engineering, Sichuan University, Chengdu 610065, China;* orcid.org/0000-0002-6872-2240; Email: chong.cheng@scu.edu.cn

Authors

Yuting Deng − *College of Polymer Science and Engineering, Med-X Center for Materials, State Key Laboratory of Polymer Materials Engineering, Sichuan University, Chengdu 610065, China;* orcid.org/0000-0002-9512-756X

https://doi.org/10.1021/acsnano.2c11448
ACS Nano 2023, 17, 2943−2957

Yang Gao − *College of Polymer Science and Engineering, Med-X Center for Materials, State Key Laboratory of Polymer Materials Engineering, Sichuan University, Chengdu 610065, China; Department of Endocrinology, Hospital of Chengdu University of Traditional Chinese Medicine, Chengdu 610072, China;* orcid.org/0000-0002-1190-4561

Tiantian Li − *College of Polymer Science and Engineering, Med-X Center for Materials, State Key Laboratory of Polymer Materials Engineering, Sichuan University, Chengdu 610065, China;* orcid.org/0000-0001-5706-0096

Sutong Xiao − *College of Polymer Science and Engineering, Med-X Center for Materials, State Key Laboratory of Polymer Materials Engineering, Sichuan University, Chengdu 610065, China;* orcid.org/0000-0002-6050-8039

Mohsen Adeli − *Department of Organic Chemistry, Lorestan University, Khorramabad 6815144316, Iran;* orcid.org/0000-0001-6895-8491

Raul D. Rodriguez − *Tomsk Polytechnic University, 634034 Tomsk, Russia;* orcid.org/0000-0003-4016-1469

Changsheng Zhao − *College of Polymer Science and Engineering, Med-X Center for Materials, State Key Laboratory of Polymer Materials Engineering, Sichuan University, Chengdu 610065, China;* orcid.org/0000-0002-4619-3499

Complete contact information is available at: https://pubs.acs.org/10.1021/acsnano.2c11448

Author Contributions

[⊥]Y.D. and Y.G. contributed equally to this work. Y.D. synthesized all the materials and performed the structural analysis. Y.G. performed the biological experiments and analyzed the corresponding results. Y.D., Y.G., T.L, S.X., M.A., and R.D.R assisted with the figure production and experiment design. Y.D., W.G., and C.C. designed and conducted the theoretical calculation. Y.D., Y.G., W.G., Q.C., C.C., and C.Z wrote and edited the manuscript.

Notes

The authors declare no competing financial interest.

ACKNOWLEDGMENTS

This work was financially supported by the National Key R&D Program of China (2019YFA0110600 and 2019YFA0110601), the National Natural Science Foundations of China (52161145402, 52173133), the 1·3·5 Project for Disciplines of Excellence, West China Hospital, Sichuan University (No. ZYJC21047), the innovation project of Med-X Center for Materials, Sichuan University (No. MCM202102), the State Key Laboratory of Polymer Materials Engineering (Grant No. sklpme2021-4-02), and Fundamental Research Funds for the Central Universities. The authors gratefully acknowledge Dr. Mi Zhou and Dr. Chao He for the analytical support, and the authors also thank Li Li, Fei Chen, and Chunjuan Bao of the Institute of Clinical Pathology, Sichuan University, for processing histological staining. The authors also acknowledge the contribution of Iran National Science Foundation: INSF under joint proposal number 4001281.

REFERENCES

(1) Matoori, S.; Veves, A.; Mooney, D. J. Advanced Bandages for Diabetic Wound Healing. *Sci. Transl. Med.* **2021**, *13*, No. eabe4839.

(2) Xie, S.; Huang, K.; Peng, J. W.; Liu, Y.; Cao, W. X.; Zhang, D. D.; Li, X. H. Self-Propelling Nanomotors Integrated with Biofilm Microenvironment-Activated NO Release to Accelerate Healing of Bacteria-Infected Diabetic Wounds. *Adv. Healthcare Mater.* **2022**, *11*, 2201323.

(3) Raziyeva, K.; Kim, Y.; Zharkinbekov, Z.; Kassymbek, K.; Jimi, S.; Saparov, A. Immunology of Acute and Chronic Wound Healing. *Biomolecules* **2021**, *11*, 700.

(4) Wong, S. L.; Demers, M.; Martinod, K.; Gallant, M.; Wang, Y. M.; Goldfine, A. B.; Kahn, C. R.; Wagner, D. D. Diabetes Primes Neutrophils to Undergo Netosis, Which Impairs Wound Healing. *Nat. Med.* **2015**, *21*, 815.

(5) Xi, Y.; Ge, J.; Wang, M.; Chen, M.; Niu, W.; Cheng, W.; Xue, Y.; Lin, C.; Lei, B. Bioactive Anti-Inflammatory, Antibacterial, Antioxidative Silicon-Based Nanofibrous Dressing Enables Cutaneous Tumor Photothermo-Chemo Therapy and Infection-Induced Wound Healing. *ACS Nano* **2020**, *14*, 2904−2916.

(6) Catrina, S. B.; Zheng, X. W. Hypoxia and Hypoxia-Inducible Factors in Diabetes and Its Complications. *Diabetologia* **2021**, *64*, 709−716.

(7) Ma, W. J.; Zhang, X. X.; Liu, Y. X.; Fan, L.; Gan, J. J.; Liu, W. L.; Zhao, Y. J.; Sun, L. Y. Polydopamine Decorated Microneedles with Fe-MSC-Derived Nanovesicles Encapsulation for Wound Healing. *Adv. Sci.* **2022**, *9*, 2103317.

(8) Tu, C. X.; Lu, H. D.; Zhou, T.; Zhang, W. Y.; Deng, L. W.; Cao, W. B.; Yang, Z. J.; Wang, Z. L.; Wu, X. Y.; Ding, J.; Xu, F.; Gao, C. Y. Promoting the Healing of Infected Diabetic Wound by an Anti-Bacterial and Nano-Enzyme-Containing Hydrogel with Inflammation-Suppressing, ROS-Scavenging, Oxygen and Nitric Oxide-Generating Properties. *Biomaterials* **2022**, *286*, 121597.

(9) Watanabe, T.; Okitsu, T.; Ozawa, F.; Nagata, S.; Matsunari, H.; Nagashima, H.; Nagaya, M.; Teramae, H.; Takeuchi, S. Millimeter-Thick Xenoislet-Laden Fibers as Retrievable Transplants Mitigate Foreign Body Reactions for Long-Term Glycemic Control in Diabetic Mice. *Biomaterials* **2020**, *255*, 120162.

(10) Londahl, M. Hyperbaric Oxygen Therapy as Treatment of Diabetic Foot Ulcers. *Diabetes-Metab. Res.* **2012**, *28*, 78−84.

(11) Yang, J. X.; Zeng, W. N.; Xu, P.; Fu, X. X.; Yu, X. J.; Chen, L.; Leng, F.; Yu, C.; Yang, Z. Y. Glucose-Responsive Multifunctional Metal-Organic Drug-Loaded Hydrogel for Diabetic Wound Healing. *Acta Biomater.* **2022**, *140*, 206−218.

(12) Zhang, Y.; Xu, K.; Zhi, D.; Qian, M.; Liu, K.; Shuai, Q.; Qin, Z.; Xie, J.; Wang, K.; Yang, J. Improving Vascular Regeneration Performance of Electrospun Poly (E-Caprolactone) Vascular Grafts Via Synergistic Functionalization with Ve-Cadherin/Vegf. *Adv. Fiber Mater.* **2022**, *4*, 1685−1702.

(13) Saw, P. E.; Zhang, Z.; Chen, Y. Y.; Li, S. L.; Huang, L. Z.; Zhang, C.; Zhao, Q. Q.; Xu, X. D.; Xiang, Q. L. ROS-Scavenging Hybrid Hydrogel for Genetically Engineered Stem Cell Delivery and Limb Ischemia Therapy. *Chem. Eng. J.* **2021**, *425*, 131504.

(14) Ma, T. F.; Zhai, X. Y.; Huang, Y. K.; Zhang, M. Z.; Zhao, X. L.; Du, Y. P.; Yan, C. H. A Smart Nanoplatform with Photothermal Antibacterial Capability and Antioxidant Activity for Chronic Wound Healing. *Adv. Healthcare Mater.* **2021**, *10*, 2100033.

(15) Dai, Z.; Wang, Q. Y.; Tang, J.; Qu, R.; Wu, M.; Li, H. Z.; Yang, Y. N.; Zhen, X.; Yu, C. Z. A Sub-6 nm $MnFe_2O_4$-Dichloroacetic Acid Nanocomposite Modulates Tumor Metabolism and Catabolism for Reversing Tumor Immunosuppressive Microenvironment and Boosting Immunotherapy. *Biomaterials* **2022**, *284*, 121533.

(16) Chen, W.; Shen, X.; Hu, Y.; Xu, K.; Ran, Q.; Yu, Y.; Dai, L.; Yuan, Z.; Huang, L.; Shen, T.; et al. Surface Functionalization of Titanium Implants with Chitosan-Catechol Conjugate for Suppression of ROS-Induced Cells Damage and Improvement of Osteogenesis. *Biomaterials* **2017**, *114*, 82−96.

(17) Han, J.; Kim, Y. S.; Lim, M.-Y.; Kim, H. Y.; Kong, S.; Kang, M.; Choo, Y. W.; Jun, J. H.; Ryu, S.; Jeong, H.-y.; et al. Dual Roles of Graphene Oxide to Attenuate Inflammation and Elicit Timely Polarization of Macrophage Phenotypes for Cardiac Repair. *ACS Nano* **2018**, *12*, 1959−1977.

(18) Yang, B.; Chen, Y.; Shi, J. Reactive Oxygen Species (ROS)-Based Nanomedicine. *Chem. Rev.* **2019**, *119*, 4881−4985.

(19) Tang, Q.; Cao, S.; Ma, T.; Xiang, X.; Luo, H.; Borovskikh, P.; Rodriguez, R. D.; Guo, Q.; Qiu, L.; Cheng, C. Engineering Biofunctional Enzyme-Mimics for Catalytic Therapeutics and Diagnostics. *Adv. Funct. Mater.* **2021**, *31*, 2007475.
(20) Brannon, E. R.; Guevara, M. V.; Pacifici, N. J.; Lee, J. K.; Lewis, J. S.; Eniola-Adefeso, O. Polymeric Particle-Based Therapies for Acute Inflammatory Diseases. *Nat. Rev. Mater.* **2022**, *7*, 796−813.
(21) Zhang, C.; Wang, H.; Yang, X.; Fu, Z.; Ji, X.; Shi, Y.; Zhong, J.; Hu, W.; Ye, Y.; Wang, Z.; et al. Oral Zero-Valent-Molybdenum Nanodots for Inflammatory Bowel Disease Therapy. *Sci. Adv.* **2022**, *8*, No. eabp9882.
(22) Mu, X.; Wang, J.; He, H.; Li, Q.; Yang, B.; Wang, J.; Liu, H.; Gao, Y.; Ouyang, L.; Sun, S.; et al. An Oligomeric Semiconducting Nanozyme with Ultrafast Electron Transfers Alleviates Acute Brain Injury. *Sci. Adv.* **2021**, *7*, No. eabk1210.
(23) Wang, Z.; You, W.; Wang, W.; Tian, W.; Chen, F.; Xiao, Y.; Chen, Y.; Wang, X. Dihydromyricetin-Incorporated Multilayer Nanofibers Accelerate Chronic Wound Healing by Remodeling the Harsh Wound Microenvironment. *Adv. Fiber Mater.* **2022**, *4*, 1556−1571.
(24) Chen, F.; Tang, Q.; Ma, T.; Zhu, B.; Wang, L.; He, C.; Luo, X.; Cao, S.; Ma, L.; Cheng, C. Structures, Properties, and Challenges of Emerging 2D Materials in Bioelectronics and Biosensors. *InfoMat* **2022**, *4*, No. e12299.
(25) Mu, S.; Deng, Y.; Xing, Z.; Rong, X.; He, C.; Cao, S.; Ma, T.; Cheng, C.; Wang, Y. Ir Cluster-Anchored Mofs as Peroxidase-Mimetic Nanoreactors for Diagnosing Hydrogen Peroxide-Related Biomarkers. *ACS Appl. Mater. Interfaces* **2022**, *14*, 56635−56643.
(26) Wang, L.; Zhu, B.; Deng, Y.; Li, T.; Tian, Q.; Yuan, Z.; Ma, L.; Cheng, C.; Guo, Q.; Qiu, L. Biocatalytic and Antioxidant Nanostructures for ROS Scavenging and Biotherapeutics. *Adv. Funct. Mater.* **2021**, *31*, 2101804.
(27) Huang, Y.; Ren, J.; Qu, X. Nanozymes: Classification, Catalytic Mechanisms, Activity Regulation, and Applications. *Chem. Rev.* **2019**, *119*, 4357−4412.
(28) Winterbourn, C. C. Reconciling the Chemistry and Biology of Reactive Oxygen Species. *Nat. Chem. Biol.* **2008**, *4*, 278−286.
(29) Wu, J. J. X.; Wang, X. Y.; Wang, Q.; Lou, Z. P.; Li, S. R.; Zhu, Y. Y.; Qin, L.; Wei, H. Nanomaterials with Enzyme-Like Characteristics (Nanozymes): Next-Generation Artificial Enzymes (II). *Chem. Soc. Rev.* **2019**, *48*, 1004−1076.
(30) Sun, Y.; Mu, S.; Xing, Z.; Guo, J.; Wu, Z.; Yu, F.; Bai, M.; Han, X.; Cheng, C.; Ye, L. Catalase-Mimetic Artificial Biocatalysts with Ru Catalytic Centers for ROS Elimination and Stem-Cell Protection. *Adv. Mater.* **2022**, *34*, 2206208.
(31) Tian, Q.; Wang, W.; Cao, L.; Tian, X.; Tian, G.; Chen, M.; Ma, L.; Liu, X.; Yuan, Z.; Cheng, C.; et al. Multifaceted Catalytic ROS-Scavenging Via Electronic Modulated Metal Oxides for Regulating Stem Cells Fates. *Adv. Mater.* **2022**, *34*, 2207275.
(32) Dai, Z.; Wang, Q.; Tang, J.; Wu, M.; Li, H.; Yang, Y.; Zhen, X.; Yu, C. J. B. Immune-Regulating Bimetallic Metal-Organic Framework Nanoparticles Designed for Cancer Immunotherapy. *Biomaterials* **2022**, *280*, 121261.
(33) Yang, J.; Zhang, R.; Zhao, H.; Qi, H.; Li, J.; Li, J. F.; Zhou, X.; Wang, A.; Fan, K.; Yan, X. Bioinspired Copper Single-Atom Nanozyme as a Superoxide Dismutase-Like Antioxidant for Sepsis Treatment. *Exploration*; Wiley Online Library, 2022; Vol. *2*, p 20210267.
(34) Dong, J.; Song, L.; Yin, J.-J.; He, W.; Wu, Y.; Gu, N.; Zhang, Y. Co_3O_4 Nanoparticles with Multi-Enzyme Activities and Their Application in Immunohistochemical Assay. *ACS Appl. Mater. Interfaces* **2014**, *6*, 1959−1970.
(35) Li, L.; Xiao, B.; Mu, J.; Zhang, Y.; Zhang, C.; Cao, H.; Chen, R.; Patra, H. K.; Yang, B.; Feng, S.; et al. A MnO_2 Nanoparticle-Dotted Hydrogel Promotes Spinal Cord Repair Via Regulating Reactive Oxygen Species Microenvironment and Synergizing with Mesenchymal Stem Cells. *ACS Nano* **2019**, *13*, 14283−14293.
(36) Han, S. I.; Lee, S. w.; Cho, M. G.; Yoo, J. M.; Oh, M. H.; Jeong, B.; Kim, D.; Park, O. K.; Kim, J.; Namkoong, E.; et al. Epitaxially Strained CeO_2/Mn_3O_4 Nanocrystals as an Enhanced Antioxidant for Radioprotection. *Adv. Mater.* **2020**, *32*, 2001566.
(37) Muhammad, F.; Huang, F.; Cheng, Y.; Chen, X.; Wang, Q.; Zhu, C.; Zhang, Y.; Yang, X.; Wang, P.; Wei, H. Nanoceria as an Electron Reservoir: Spontaneous Deposition of Metal Nanoparticles on Oxides and Their Anti-Inflammatory Activities. *ACS Nano* **2022**, *16*, 20567−20576.
(38) Yan, R.; Sun, S.; Yang, J.; Long, W.; Wang, J.; Mu, X.; Li, Q.; Hao, W.; Zhang, S.; Liu, H.; et al. Nanozyme-Based Bandage with Single-Atom Catalysis for Brain Trauma. *ACS Nano* **2019**, *13*, 11552−11560.
(39) Wang, Z. Z.; Wu, J. X.; Zheng, J. J.; Shen, X. M.; Yan, L.; Wei, H.; Gao, X. F.; Zhao, Y. L. Accelerated Discovery of Superoxide-Dismutase Nanozymes Via High-Throughput Computational Screening. *Nat. Commun.* **2021**, *12*, 6866.
(40) Liu, H. L.; Li, Y. H.; Sun, S.; Xin, Q.; Liu, S. H.; Mu, X. Y.; Yuan, X.; Chen, K.; Wang, H.; Varga, K.; Mi, W. B.; Yang, J.; Zhang, X. D. Catalytically Potent and Selective Clusterzymes for Modulation of Neuroinflammation through Single-Atom Substitutions. *Nat. Commun.* **2021**, *12*, 114.
(41) Yang, B. W.; Yao, H. L.; Yang, J. C.; Chen, C.; Shi, J. L. Construction of a Two-Dimensional Artificial Antioxidase for Nanocatalytic Rheumatoid Arthritis Treatment. *Nat. Commun.* **2022**, *13*, 1988.
(42) Ai, Y. J.; Hu, Z. N.; Liang, X. P.; Sun, H. B.; Xin, H. B.; Liang, Q. L. Recent Advances in Nanozymes: From Matters to Bioapplications. *Adv. Funct. Mater.* **2022**, *32*, 2110432.
(43) Deng, Y. T.; Xiao, S. T.; Zheng, Y. J.; Rong, X.; Bai, M. R.; Tang, Y. J.; Ma, T.; Cheng, C.; Zhao, C. S. Emerging Electrocatalytic Activities in Transition Metal Selenides: Synthesis, Electronic Modulation, and Structure-Performance Correlations. *Chem. Eng. J.* **2023**, *451*, 138514.
(44) Yang, D. X.; Zhu, Q. G.; Chen, C. J.; Liu, H. Z.; Liu, Z. M.; Zhao, Z. J.; Zhang, X. Y.; Liu, S. J.; Han, B. X. Selective Electroreduction of Carbon Dioxide to Methanol on Copper Selenide Nanocatalysts. *Nat. Commun.* **2019**, *10*, 677.
(45) Zhao, Y. M.; Cong, H. J.; Li, P.; Wu, D.; Chen, S. L.; Luo, W. Hexagonal $RuSe_2$ Nanosheets for Highly Efficient Hydrogen Evolution Electrocatalysis. *Angew. Chem., Int. Ed.* **2021**, *60*, 7013−7017.
(46) Wang, K. F.; Li, B.; Wei, W.; Wang, J. G.; Shen, Q.; Qu, P. Excessive Se on $RuSe_2$ Nanocrystals to Accelerate Water Dissociation for the Enhanced Electrocatalytic Hydrogen Evolution Reaction. *Nanoscale* **2020**, *12*, 23740−23747.
(47) Yun, X. R.; Wu, S. L.; Li, J. Y.; Li, L. S.; Zhou, J.; Lu, P. C.; Tang, H.; Zhu, Y. R. Facile Synthesis of Crystalline $RuSe_2$ Nanoparticles as a Novel Pseudocapacitive Electrode Material for Supercapacitors. *Chem. Commun.* **2019**, *55*, 12320−12323.
(48) Jiang, K.; Liu, B. Y.; Luo, M.; Ning, S. C.; Peng, M.; Zhao, Y.; Lu, Y. R.; Chan, T. S.; de Groot, F. M. F.; Tan, Y. W. Single Platinum Atoms Embedded in Nanoporous Cobalt Selenide as Electrocatalyst for Accelerating Hydrogen Evolution Reaction. *Nat. Commun.* **2019**, *10*, 1743.
(49) Guo, C. X.; Zheng, Y.; Ran, J. R.; Xie, F. X.; Jaroniec, M.; Qiao, S. Z. Engineering High-Energy Interfacial Structures for High-Performance Oxygen-Involving Electrocatalysis. *Angew. Chem., Int. Ed.* **2017**, *56*, 8539−8543.
(50) Dou, Y. H.; He, C. T.; Zhang, L.; Yin, H. J.; Al-Mamun, M.; Ma, J. M.; Zhao, H. J. Approaching the Activity Limit of $CoSe_2$ for Oxygen Evolution Via Fe Doping and Co Vacancy. *Nat. Commun.* **2020**, *11*, 1664.
(51) Zheng, Y. R.; Gao, M. R.; Gao, Q.; Li, H. H.; Xu, J.; Wu, Z. Y.; Yu, S. H. An Efficient $CeO_2/CoSe_2$ Nanobelt Composite for Electrochemical Water Oxidation. *Small* **2015**, *11*, 182−188.
(52) Deng, J.; Li, H. B.; Xiao, J. P.; Tu, Y. C.; Deng, D. H.; Yang, H. X.; Tian, H. F.; Li, J. Q.; Ren, P. J.; Bao, X. H. Triggering the Electrocatalytic Hydrogen Evolution Activity of the Inert Two-Dimensional MoS_2 Surface Via Single-Atom Metal Doping. *Energy Environ. Sci.* **2015**, *8*, 1594−1601.

https://doi.org/10.1021/acsnano.2c11448
ACS Nano 2023, 17, 2943−2957

(53) Kang, S.; Gil, Y. G.; Min, D. H.; Jang, H. Nonrecurring Circuit Nanozymatic Enhancement of Hypoxic Pancreatic Cancer Phototherapy Using Speckled Ru-Te Hollow Nanorods. *ACS Nano* **2020**, *14*, 4383−4394.
(54) Liu, T. F.; Xiao, B. W.; Xiang, F.; Tan, J. L.; Chen, Z.; Zhang, X. R.; Wu, C. Z.; Mao, Z. W.; Luo, G. X.; Chen, X. Y.; Deng, J. Ultrasmall Copper-Based Nanoparticles for Reactive Oxygen Species Scavenging and Alleviation of Inflammation Related Diseases. *Nat. Commun.* **2020**, *11*, 2788.
(55) Imlay, J. A.; Linn, S. DNA Damage and Oxygen Radical Toxicity. *Science* **1988**, *240*, 1302−1309.
(56) Denu, R. A.; Hematti, P. Effects of Oxidative Stress on Mesenchymal Stem Cell Biology. *Oxid. Med. Cell. Longev.* **2016**, *2016*, 2989076.
(57) Paluch, E. K.; Aspalter, I. M.; Sixt, M. Focal Adhesion-Independent Cell Migration. *Annu. Rev. Cell Dev. Bi.* **2016**, *32*, 469−490.
(58) Parsons, J. T.; Martin, K. H.; Slack, J. K.; Taylor, J. M.; Weed, S. A. Focal Adhesion Kinase: A Regulator of Focal Adhesion Dynamics and Cell Movement. *Oncogene* **2000**, *19*, 5606−5613.
(59) Wang, C. G.; Li, Y.; Yang, M.; Zou, Y. H.; Liu, H. H.; Liang, Z. Y.; Yin, Y.; Niu, G. C.; Yan, Z. G.; Zhang, B. H. Efficient Differentiation of Bone Marrow Mesenchymal Stem Cells into Endothelial Cells in Vitro. *Eur. J. Vasc. Endovasc.* **2018**, *55*, 257−265.
(60) Arnaoutova, I.; George, J.; Kleinman, H. K.; Benton, G. The Endothelial Cell Tube Formation Assay on Basement Membrane Turns 20: State of the Science and the Art. *Angiogenesis* **2009**, *12*, 267−274.
(61) O'Loughlin, A.; Kulkarni, M.; Creane, M.; Vaughan, E. E.; Mooney, E.; Shaw, G.; Murphy, M.; Dockery, P.; Pandit, A.; O'Brien, T. Topical Administration of Allogeneic Mesenchymal Stromal Cells Seeded in a Collagen Scaffold Augments Wound Healing and Increases Angiogenesis in the Diabetic Rabbit Ulcer. *Diabetes* **2013**, *62*, 2588−2594.
(62) Kim, H. S.; Sun, X. Y.; Lee, J. H.; Kim, H. W.; Fu, X. B.; Leong, K. W. Advanced Drug Delivery Systems and Artificial Skin Grafts for Skin Wound Healing. *Adv. Drug Deliver. Rev.* **2019**, *146*, 209−239.

https://doi.org/10.1021/acsnano.2c11448
ACS Nano 2023, 17, 2943−2957